Ordered Mesoporous Thin Film Ferroelectrics of Biaxially Textured Lead Zirconate Titanate (PZT) by Chemical Solution Deposition

Christian Reitz, Philipp M. Leufke, Horst Hahn, and Torsten Brezesinski[*]

Institute of Nanotechnology, Karlsruhe Institute of Technology, Hermann–von–Helmholtz–Platz 1, 76344 Eggenstein–Leopoldshafen, Germany.

Abstract

Lead zirconate titanate (PZT) thin film nanostructures with a high degree of biaxial texturing and good ferroelectric properties have been prepared by facile chemical solution deposition on (001)–oriented STO:Nb and LSMO/STO:Nb substrates using a poly(ethylene–*co*–butylene)–*block*–poly(ethylene oxide) diblock copolymer as structure–directing agent. The samples were thoroughly characterized by electron microscopy, synchrotron–based grazing incidence small–angle X–ray scattering, X–ray diffraction (including θ–2θ, ω, and φ scans), X–ray photoelectron spectroscopy, time–of–flight secondary ion mass spectrometry, and by ferroelectric polarization switching and fatigue measurements. We show that (1) the cubic mesostructured films with 16 nm diameter pores can be crystallized to produce single phase perovskite PZT with retention of nanoscale order, (2) the sol–gel derived material has an in–plane texture of ~1.9° and an out–of–plane texture of ~1.5°, and (3) the top surface is Zr–rich (the composition in the interior of the films is closer to the targeted composition of $PbZr_{0.52}Ti_{0.48}O_3$). The coercive field and remanent polarization of approx. 100 nm–thick films derived from dynamic *P*–*E* experiments are ~250 kV cm^{-1} and ~25 μC cm^{-2} (~7 μC cm^{-2} after subtracting the non–switching components). Despite the use of Au top electrodes, the nanocrystalline samples show reasonable fatigue performance. All these features render the mesoporous PZT thin films attractive, e.g., for producing strain–coupled composite multiferroics.

Keywords

Ferroelectrics, sol–gel chemistry, self–assembly, perovskite, epitaxy, mesoporous

Introduction

Despite the efforts to move towards lead–free electronics over the past years,[1,2] lead zirconate titanate ($PbZr_{1-x}Ti_xO_3$, PZT) still plays a major role in the electroceramics industry today. Ferro– or piezoelectric materials in thin film format are widely used in non–volatile random–access memory (NVRAM), dynamic random–access memory (DRAM), micro–electro–mechanical systems (MEMS), and other devices.[3–7] For example, applications of high performance piezoelectric MEMS include transducers, actuators, micro–pumps, and inkjet printheads, to mention only a few.[8–12]

PZT materials, in particular, have been shown to outperform many other piezoelectrics, which is due in part to the large room–temperature electromechanical coupling factors.[13,14] The maximum values of the latter coupling factors, the piezoelectric coefficients, and the dielectric permittivity occur in the immediate vicinity of the so–called morphotropic phase boundary (Zr/Ti = 52/48).[15,16] This boundary results from the metastable coexistence of the tetragonal and rhombohedral phases with six and eight equivalent polarization directions, respectively.[17]

Research over the past several decades has demonstrated that the ferroelectric behavior of PZT thin films can be strongly affected by the choice of the top and bottom electrodes, the Zr/Ti ratio, and by the deposition method used.[18,19] However, the microstructure, texture, film thickness, and other parameters also have significant effects on the electrical polarization properties.[20–22] Among other things, it has been shown that the use of $La_{1-y}Sr_yMnO_3/SrTiO_3$:Nb heterostructure substrates – referred to as LSMO/STO:Nb in the following – instead of bare STO:Nb single crystal substrates as back electrodes is beneficial for preventing polarization loss due to leakage.[23,24] The reason for this can be found in the conduction mechanisms of the electrode materials with LSMO and STO:Nb being p–type and n–type conductors, respectively, and the

fact that PZT can be regarded as a wide bandgap p–type semiconductor. Thus, the electrode–ferroelectric interface junctions are much more favorable for the PZT/LSMO than PZT/STO:Nb.[25,26]

In the present work, we describe for the first time the fabrication of ordered mesoporous thin film ferroelectrics of single phase perovskite PZT on (001)–oriented STO:Nb and LSMO/STO:Nb substrates via facile solution–phase co–assembly of ordinary sol–gel precursors with a poly(ethylene–*co*–butylene)–*block*–poly(ethylene oxide) diblock copolymer.[27] In this evaporation–induced self–assembly (EISA) synthesis,[28,29] the organic polymer, which is also referred to as KLE,[30] acts as structure–directing agent. In recent years, we have shown that KLE has superior templating properties and produces nanostructured materials with large ordering lengths.[31,32] The latter is a major advantage as such materials can be more easily crystallized while retaining the porosity and periodicity. Both the requirements on polymer structure–directing agents in general and the fundamental principles of self–assembly and soft–templating have been described in excellent reviews elsewhere and, therefore, are not discussed here.[33–42]

Apart from the synthesis, we show that the KLE–templated PZT thin films exhibit good ferroelectric properties and further have a high degree of biaxial texturing, that is, they possess both in–plane and out–of–plane preferred orientations. Biaxial alignment is common in sol–gel derived (bulk) materials deposited on single crystal substrates, but is unique for polymer–templated ordered mesoporous metal oxide films. This property alone makes the samples employed in this work interesting for fundamental studies. Here, we use the mesoporous nanocrystalline PZT as a model system to examine the influence of the morphology and microstructure on the polarization switching and fatigue behavior relative to bulk thin films. Overall, we believe that the integration of mesoporosity with texture–specific properties paves

the way to broaden the scope of application of this and other related materials (e.g., due to the wealth of novel opportunities for device design).

Experimental Section

Materials: $Pb(OAc)_2 \times 3H_2O$ (99.99%), $Ti(^iOPr)_4$ (99.99%), $Zr(OBu)_4$ (80 wt.–% in butanol), glacial acetic acid (99.99%), absolute ethanol, and 2–methoxyethanol were purchased from Sigma–Aldrich and ABCR, respectively. Polished 0.5 wt.–% Nb–doped $SrTiO_3$ (STO:Nb) single crystal substrates with (001) orientation and a total area of 0.5×1.0 cm^2 were purchased from SurfaceNet GmbH, Germany. $La_{0.83}Sr_{0.17}MnO_3$/STO:Nb (LSMO/STO:Nb) heterostructure substrates were prepared by large–distance radio frequency (rf) magnetron sputtering.[43] In brief, optimal conditions include both a substrate temperature of ~780 °C and an oxygen–to–argon ratio of 40% (O_2/Ar+O_2), with a working pressure of 1.8 Pa. After LSMO deposition, the heterostructure substrates were cooled to room–temperature in pure oxygen. $H[(CH_2CH_2)_{0.67}(CH_2CHCH_2CH_3)_{0.33}]_{89}(OCH_2CH_2)_{79}OH$ (KLE) was used as polymer structure–directing agent in this work.[30,44] This polymer was synthesized by anionic polymerization of ethylene oxide using a "Kraton Liquid"–type *ω*–hydroxypoly(ethylene–*co*–butylene) precursor polymer as macroinitiator.[44]

Thin Film Synthesis: A solution made from 50 mg of KLE, 1.5 mL of ethanol, 0.15 mL of glacial acetic acid, and 0.6 mL of 2–methoxyethanol is combined with 137 mg of $Pb(OAc)_2 \times 3H_2O$ (10% excess to compensate for lead loss during thermal annealing at elevated temperatures), 44 mg of $Ti(^iOPr)_4$, and 82 mg of $Zr(OBu)_4$ in butanol. After stirring the slightly opaque solution for 30 min – micellar aggregates are already present because of the low cmc of the large diblock copolymer KLE – thin films can be deposited via dip coating on (001)–oriented

STO:Nb and LSMO/STO:Nb substrates. Optimal conditions include room–temperature relative humidities of 18–22% and constant withdrawal rates of 5–10 mm s^{-1}. For best results, the as–made films are directly transferred to an oven at 140 °C for 15 min and then heated to 300 °C using a 90 min ramp followed by aging for 12 h. Finally, the films are heated to 650 °C at a rate of 10 °C min^{-1} followed by aging for 5 min and subsequent quenching to room–temperature.

Characterization Methods: Bright–field transmission electron microscopy (TEM) and field–emission scanning electron microscopy (FESEM) images were taken with a CM30–ST from Philips at 300 kV and a MERLIN from Carl Zeiss at 5 kV, respectively. X–ray reflectivity (XRR) and high–resolution X–ray diffraction (HRXRD) measurements were carried out on a Bruker D8 Discover diffractometer equipped with a Ge(022)×4 asymmetric monochromator (λ = 0.15418 nm, sample–to–detector distance = 26 cm) and a PathFinder scintillation point detector. Grazing incidence small–angle X–ray scattering (GISAXS) patterns were collected at the German synchrotron radiation facility HASYLAB at DESY on beamline BW4 (λ = 0.1381 nm, beam size = 23 μm (vertical) × 30 μm (horizontal), incident angle = 0.2°, sample–to–detector distance = 1779 mm,) using a MarCCD area detector (pixel size = 79 μm, resolution = 2.03×10^{-3} nm^{-1} px^{-1}, counting time = 2×150 s). DPDAK 0.3.0 software was used for data analysis. X–ray photoelectron spectroscopy (XPS) spectra were acquired on a VersaProbe PHI 5000 Scanning ESCA Microprobe from Physical Electronics with monochromatic Al–Kα X–ray source and a hemispherical electron energy analyzer at an electron takeoff angle of 45°. The C 1*s* signal from adventitious hydrocarbon at 284.8 eV was used as energy reference to correct for charging. The films were also analyzed by time–of–flight secondary ion mass spectrometry (ToF–SIMS) using a ToF–SIMS 5–100 from ION–TOF GmbH. A primary beam of Bi^+ ions (E = 25 keV, I_0 = 1.84 pA, spot size = 100×100 μm^2, dose density = 2.69×10^{13} cm^{-2}) was used to generate secondary

ions. Sputter etching was carried out using a beam of O_2^+ ions (E = 1 keV, I_0 = 297.1 nA, spot size = 200×200 μm^2, dose density = 1.12×10^{18} cm^{-2}). The ferroelectric properties were analyzed using a TF Analyzer 1000 from aixACCT Systems GmbH. The film thickness was determined with an Alpha Step IQ Surface Profiler from KLA Tencor. Crystal Impact Diamond 3.2i software was used for crystal structure visualization.

Results and Discussion

In brief, in a typical synthesis, the inorganic sol–gel precursors are dissolved together with the diblock copolymer KLE in a mixed solvent of ethanol and 2–methoxyethanol. In addition, glacial acidic acid is added to the colorless solution to slow down the hydrolysis/condensation reactions or, in other words, to prevent phase separation. Thereafter, films with thicknesses in the submicrometer range can be produced via room–temperature spin or dip coating at relative humidities of 18–22%. In the present work, we used electrically conductive (001)–oriented STO:Nb and LSMO/STO:Nb both as single crystal substrates and as back electrodes. The LSMO/STO:Nb heterostructure substrates with an 11.7 nm–thick, fully strained LSMO(00*l*) buffer layer (see also X–ray reflectivity data in **Figure S1** in the Supporting Information [SI]) were prepared by rf magnetron sputtering. The experimental details are described elsewhere.[43] We note that the LSMO buffer layer has no notable effect on the self-assembly process and the microstructure of the PZT thin films. The best results in terms of pore ordering and structural homogeneity are achieved when the as–made films are directly transferred to an oven at 140 °C. This means that no elaborate treatment steps are needed prior to annealing, which helps reducing the synthesis time significantly. Lastly, the films are submitted to a straightforward multistep calcination process to stabilize the mesostructured inorganic/organic composite framework,

make the material porous, and crystallize the amorphous wall structure to obtain single phase perovskite PZT.

The nanoscale structure before (300–600 °C) and after crystallization (600–650 °C) was analyzed by a combination of field–emission scanning electron microscopy (FESEM), transmission electron microscopy (TEM), and grazing incidence small–angle X–ray scattering (GISAXS). Panels (a) and (b) of **Figure 1** show top view FESEM images of a KLE–templated PZT thin film heated at 650 °C for 5 and 10 min, respectively. It can be clearly seen that the pore structure is retained to a large extent throughout crystallization (and probably partial grain growth). However, as is evident from the data, the pore–solid architecture is much less affected after 5 min of calcination, which is the reason for choosing this thermal treatment for all films.[45] In addition, it can be seen that the top surface is crack–free on the micrometer level (see also low–magnification top view and cross–sectional FESEM images in **Figure S2** in the SI) and the pore cavities are rather uniform in size and shape with an average in–plane diameter of 16 nm. The cross–sectional FESEM image in panel (c) establishes that the network of pores persists throughout the bulk. This result is also confirmed by bright–field TEM studies. The imaging data in panel (d) show the so–gel derived material is, in fact, mesostructured with cubic pore symmetry and wall thicknesses in the range of 8–12 nm (see also TEM images at different magnifications in **Figure S2** in the SI). Overall, the microscopy results lead us to conclude that the self–assembled PZT thin films are thermally quite stable: they are well–defined at the nanometer length scale and seem free of major structural defects, making them interesting as a model system to study the ferroelectric properties of a solution–processed material that could enable novel functional device design that cannot be achieved with dense layers.

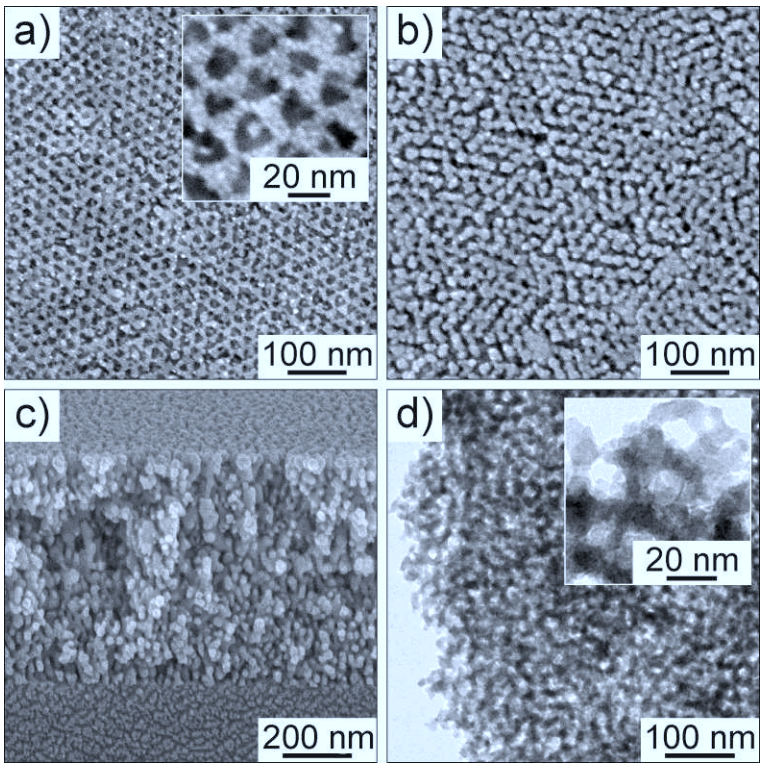

Figure 1. Morphology of KLE–templated PZT thin films heated at 650 °C for 5 min (a, c, d) and 10 min (b), respectively: (a, b) top view FESEM images at different magnifications; (c) cross–sectional FESEM image showing the pore network to persists throughout the bulk; (d) bright–field TEM images at different magnifications.

As mentioned above, the changes in nanoscale structure during thermal treatment were also followed *ex situ* by synchrotron–based GISAXS. **Figure 2** shows GISAXS patterns obtained on a KLE–templated PZT thin film heated at different annealing temperatures of 300, 500, 600, and 650 °C. In order to ensure that the GISAXS results provide reliable information about the film structure, the intensity distribution in the scattering plane from a vertical line cut ("detector scan")[46] was compared to that of conventional SAXS experiments conducted in θ–2θ geometry using a laboratory diffractometer. As can be seen in **Figure S3** in the SI, the corresponding

patterns are in good agreement showing a distinct peak at $\boldsymbol{q}_z(300\ °C) = 1.30\ nm^{-1}$; therefore, the GISAXS data are reliable and representative. From **Figure 2**, it is apparent that amorphous material produces patterns with in– and out–of–plane scattering maxima. These maxima are characteristic of a cubic mesostructure, but a clear assignment is not possible. Nevertheless, it should be noted that the top surface with primary hexagonal symmetry (see **Figure 1**) argues against a body–centered cubic structure with (110) orientation relative to the plane of the substrate. Instead, it seems more likely that the scattering maxima can be associated with the formation of a distorted (111)–oriented face–centered cubic mesophase.[47–49] Both of these structures are common in KLE–templated inorganics.[50–52] The degree of order is not as high as in other polymer–templated non–silicate thin films[32,34,42,53,54] – the vast majority are binary transition metal oxides – but the material studied in this work is rather complex from a chemical point of view in that three different sol–gel precursors were used in the synthesis. Furthermore, it can be seen that the material undergoes large unidirectional lattice contraction, namely, perpendicular to the substrate plane. This change in volume is triggered by hydrolysis/condensation and combustion reactions on heating. The very same reactions also lead to more intense in–plane signals due to a steady increase in scattering contrast ($\Delta\rho$). Lastly, the GISAXS data show that calcination at $\vartheta \geq 600$ °C is accompanied by scattering intensity loss in the $\boldsymbol{q}_z$–direction, that is, in the scattering plane. However, the lack of strong scattering after crystallization is not surprising and can be explained by structural changes in the pore network. Such changes have a more significant effect on the pore ordering in the direction perpendicular to the substrate due to the morphological anisotropy of the films with far fewer repeat units in the $\boldsymbol{q}_z$–direction.

In addition to the GISAXS patterns, line cuts along the highest intensity in the $\boldsymbol{q}_y$–direction (intensity distribution parallel to the substrate plane) are shown in **Figure 2**. These horizontal cuts provide more insight into the lateral film structure and further confirm that the in–plane lattice contraction is, in fact, negligible since there is no notable shift in the position of the first order peak at $\boldsymbol{q}_y$ = 0.26 nm^{-1} with increasing annealing temperature. The shoulder at the higher scattering vector side of the fundamental peak is presumably due to random stacking faults or, in other words, due to the presence of domains with both hexagonal and square arrays of pores, as already indicated by the micrographs in **Figure 1**.[47] Because the footprint area of the incident X–ray beam was rather large, such local inhomogeneities can be easily seen in the data. More importantly, however, the line cuts demonstrate that the lateral film ordering is affected only to a limited extent by the crystallization – even higher order maxima can still be observed very clearly. Thus, the GISAXS results corroborate the electron microscopy data, and collectively they provide ample evidence that the distorted cubic pore network is largely preserved after heating the films at 650 °C for 5 min.

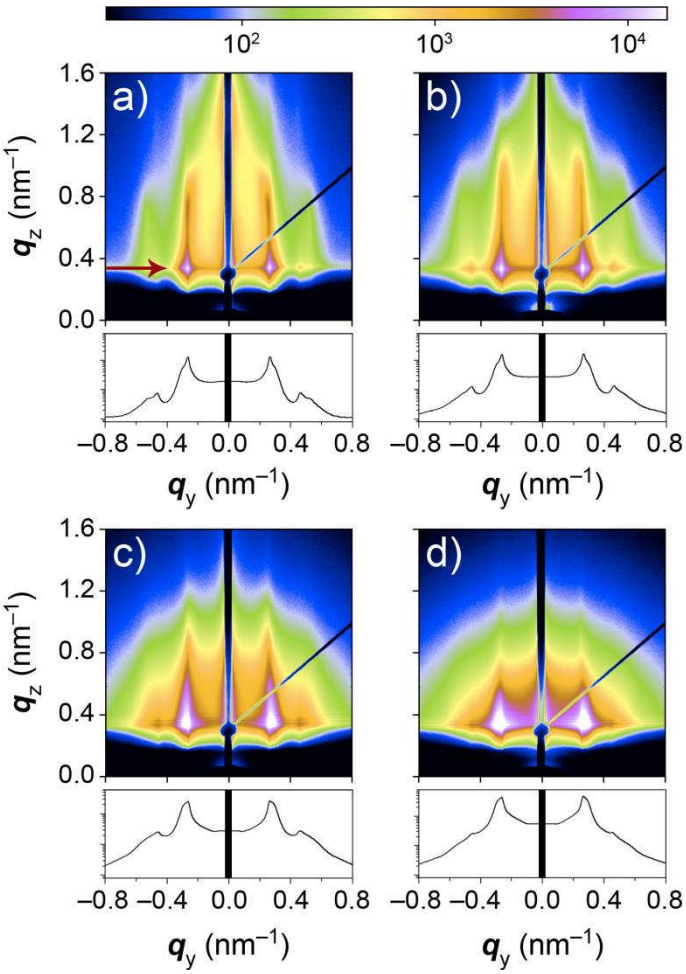

Figure 2. Synchrotron–based GISAXS patterns, with logarithmic intensity scaling, at an incident angle of 0.2° obtained after heating a KLE–templated PZT thin film at 300 °C for 12 h (a), and 500 (b), 600 (c), and 650 °C (d) for 5 min, respectively. The intensity color map is shown above. Horizontal line cuts, with 8 pixel line width, made along the highest intensity (indicated by the red arrow in panel (a)) are given below each pattern.

High–resolution X–ray diffraction (HRXRD) studies in θ–2θ geometry demonstrate the crystallinity of the KLE–templated PZT thin films. Panel (a) of **Figure 3** shows a HRXRD pattern of a film deposited on LSMO/STO:Nb heterostructure substrate. In the range of 2θ from 18° to 52°, only two peaks – namely, the (001) and (002) reflections – corresponding to the

perovskite PZT phase can be observed.[55] In addition, HRXRD indicates the epitaxial growth of single–phase, fully strained LSMO(00*l*) with lattice parameter c = 3.85 Å on (001)–oriented STO:Nb; more details are given elsewhere.[43] To better characterize the crystallinity of the mesoporous PZT with regard to texture and uniformity, both a φ scan, by tilting χ to 44.56°, on the (110) reflection and an ω scan (rocking curve measurement) on the (001) reflection at 2θ = 21.84° were conducted. The φ scan in panel (b) shows four–fold symmetry – one distinct peak every 90°.[56] The line width of the peaks as full–width at half–maximum (FWHM) was determined to be 1.9°, thereby indicating pronounced in–plane alignment. The out–of–plane alignment (degree of preferred orientation to the substrate) was estimated from the rocking curve in panel (c). These data suggest inhomogeneities throughout the bulk of the films. More specifically, curve–fitting yields two components with FWHM values of 0.05° and 1.5°. At this point, we presume that the PZT domains grow epitaxially only in the vicinity of the substrate/film interface, that is, in a limited range of film thicknesses.[57] Nevertheless, the degree of preferred orientation in [00*l*] is high, particularly, for such kind of sol–gel derived material. Taken together, the XRD results demonstrate biaxial texturing of the KLE–templated PZT heated at 650 °C for 5 min.[58] Furthermore, we find that the films are single phase with lattice parameters $a = b$ = 4.05 Å – derived from a θ–2θ scan on the (110) plane – and c = 4.07 Å, thus indicating a small tetragonal distortion ($\gamma = c/a - 1$ = 0.005). A schematic representation of the LSMO and PZT lattices viewed along the crystallographic *c*–axis is shown in the inset of **Figure 3a**.

In summary, the data in **Figures 1–3** establish that PZT thin films can be templated using the large diblock copolymer KLE and further crystallized to produce single phase material with both

a distorted cubic pore–solid architecture and strong in–plane and out–of–plane preferred orientations.

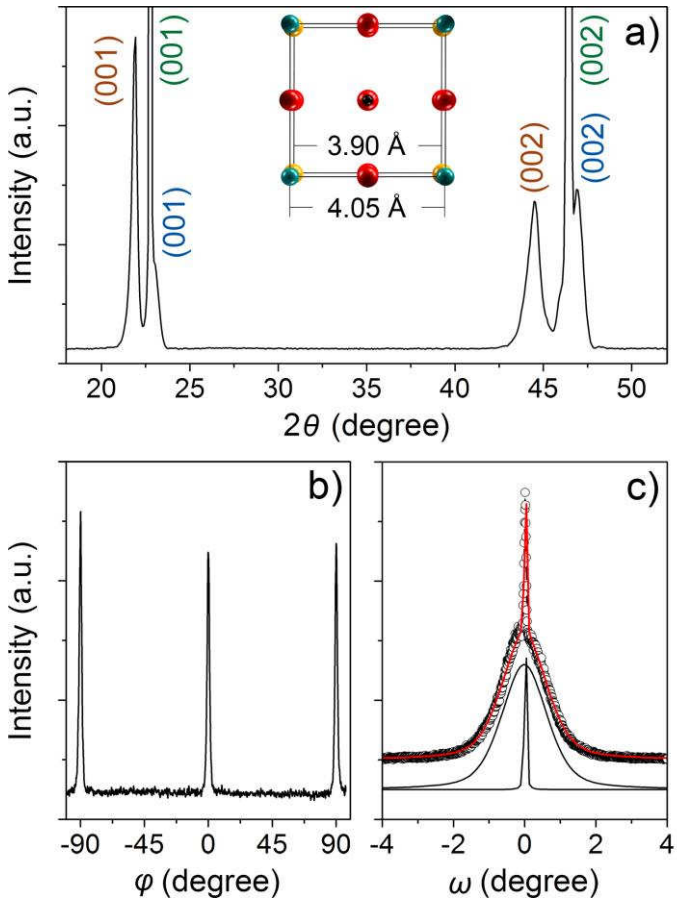

Figure 3. Crystalline structure and texture of KLE–templated PZT thin films on LSMO/STO:Nb heterostructure substrate heated at 650 °C for 5 min: (a) HRXRD pattern showing peaks for (001)–oriented STO:Nb, LSMO, and PZT in green, blue, and brown, respectively; (inset in a) schematic representation of the LSMO ($a = b = 3.90$ Å) and PZT ($a = b = 4.05$ Å) lattices viewed along the crystallographic *c*–axis with oxygen in red, lead in green, zirconium/titanium in black, and lanthanum/strontium in yellow (note that the topmost face–centered oxygen atom is not shown for clarity); (b) 200° φ scan at $\chi = 44.56°$ showing the four–fold symmetry of the (110) plane; (c) ω scan on the (001) reflection – solid lines in black are pseudo–Voigt fits to the data and the red curve corresponds to the sum of the peak fits.

To obtain information about the elemental composition and chemical state of the KLE–templated PZT thin films, a series of X–ray photoelectron spectroscopy (XPS) and time–of–flight secondary ion mass spectrometry (ToF–SIMS) measurements was carried out. The wide–scan XPS survey spectrum in panel (a) of **Figure 4** shows solely titanium, zirconium, lead, oxygen, and carbon. The presence of the latter (see C 1*s* peak) is likely due to adventitious hydrocarbon adsorbed from the atmosphere. **Figure 4** further shows detail spectra of the O 1*s*, Ti 2*p*, Zr 3*d*, and Pb 4*f* core level regions. The O 1*s* spectrum in panel (b) indicates two oxygen bonding states. The main peak centered at (529.66 ± 0.05) eV can be associated with lattice oxygen and the minor one at (531.06 ± 0.05) eV with hydroxyl groups/adsorbed water at the top surface.[59] This result is not surprising considering that the sol–gel derived films are mesoporous and were stored under ambient conditions. The Ti 2*p* spectrum in panel (c) contains a doublet due to spin–orbit splitting. As expected, we find a relative area ratio of 1:2 for the $2p_{1/2}$ and $2p_{3/2}$ photoelectron peaks at binding energies of (463.64 ± 0.05) eV and (457.94 ± 0.05) eV, respectively. Both the peak position and separation (5.70 eV) are characteristic of Ti^{4+} (in related perovskite materials).[60,61] The fact that the FWHM values are notably different for both component peaks (namely, 1.40 eV and 2.06 eV) can be explained by Coster-Kronig broadening.[62] In contrast, the Zr 3*d* spectrum in panel (d) was fitted using spin–orbit splitting parameters with equal FWHM and a relative area ratio of 2:3 for the $3d_{3/2}$ and $3d_{5/2}$ lines. In this case, the photoelectron peaks are centered at (184.28 ± 0.05) eV and (181.85 ± 0.05) eV, respectively, which is in agreement with the binding energy values reported in the literature for bulk PZT.[63] The Pb 4*f* core level region was also analyzed in detail to find out if the formation of Pb^{4+} and impurity phases, such as lead zirconate, pyrochlore, lead oxide, and others, in the

synthesis can be ruled out. The presence of second phases has been shown to have a strong and negative effect on the ferroelectric properties of PZT materials. The spectrum in panel (e) shows a single doublet with symmetric $4f_{5/2}$ and $4f_{7/2}$ peaks at (142.97 ± 0.05) eV and (138.11 ± 0.05) eV, respectively. The relative area ratio is 3:4. On the basis of these data, we conclude that the KLE–templated PZT thin films heated at 650 °C for 5 min in air are free of both Pb^{4+} and impurity phases – within the detection limit of the method.[64] The surface composition was calculated from the peak areas by using the respective atomic sensitivity factors for each core level.[65] From this analysis, we find an atomic composition, Pb/Zr/Ti = 0.88/0.66/0.46, which indicates that the top surface is Zr–rich and slightly Pb– and Ti–deficient. This result is also confirmed by ToF–SIMS. A representative ToF–SIMS profile showing the distribution of C^+, Zr^+, Ti^+, and Pb^+ as a function of depth from the top surface is given in **Figure S4** in the SI. It demonstrates that, after a sputtering depth of 15–20 nm, the ions are homogeneously distributed throughout the films, that is, the stoichiometry does not change anymore as a function of thickness, and the diblock copolymer used as structure–directing agent in this work is fully removed after calcination. Only minor amounts of hydrocarbons can be detected at the top surface, in agreement with the XPS results. Overall, ToF–SIMS suggests that the bulk chemical composition is close to the targeted atomic composition, Pb/Zr/Ti = 1/0.52/0.48. The reason why zirconium is enriched at the top surface is not yet fully understood.[66] However, given that the PZT material employed here is solution–processed via dip coating as well as nanocrystalline and mesoporous, it seems also rather well–defined at the atomic level.

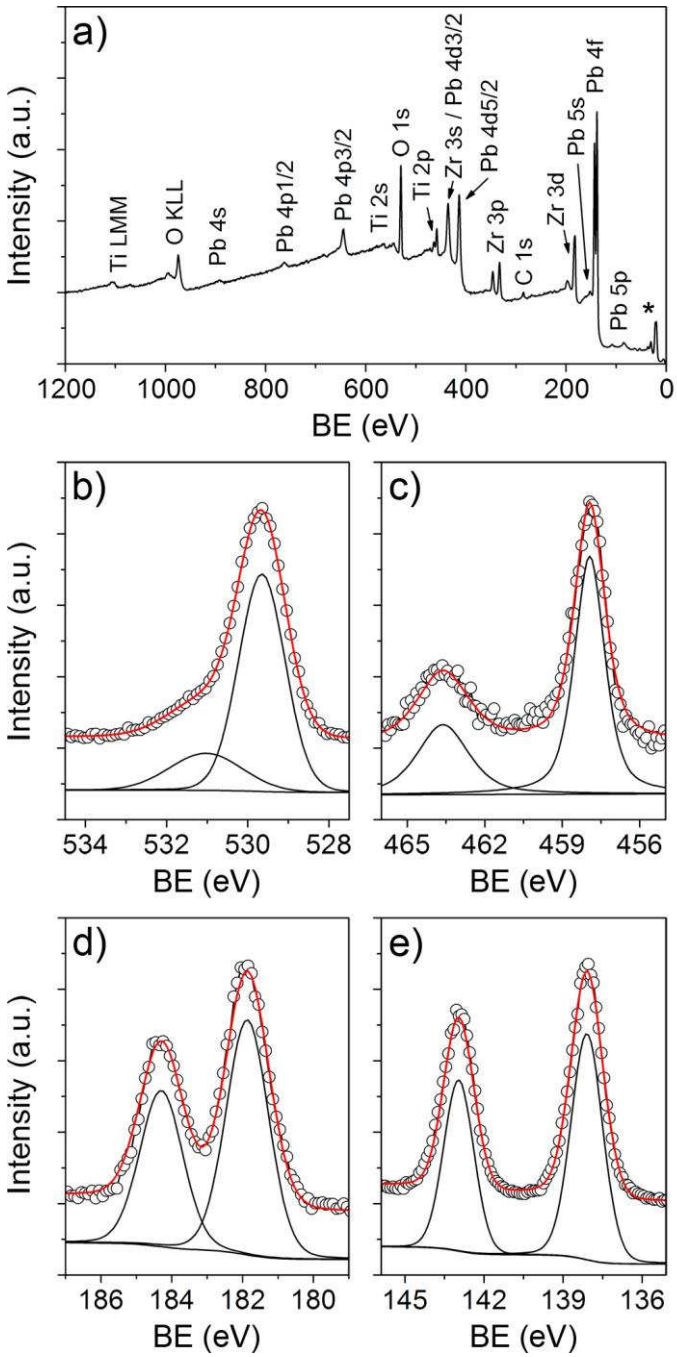

Figure 4. Elemental composition and chemical state of KLE–templated PZT thin films heated at 650 °C for 5 min in air: (a) XPS survey spectrum with the Ti 3*s*, Zr 4*s*, Zr 4*p*, O 2*s*, and Pb 5*d* levels in the binding energy (BE) range from 58 eV to 19 eV indicated by an asterisk; (b–d) XPS detail spectra of the O 1*s*, Ti 2*p*, Zr 3*d*, and Pb 4*f* regions, respectively – solid lines in black are

fits to the data and the red curves correspond to the sum of the peak fits (the Shirley method was applied to subtract backgrounds).

The room–temperature ferroelectric behavior of approx. 100 nm–thick KLE–templated PZT films on LSMO/STO:Nb heterostructure substrate with 50 nm–thick Au top electrodes was analyzed by polarization switching and fatigue experiments. As mentioned previously, the reason for the use of a thin LSMO(00*l*) buffer layer is that it helps to prevent polarization loss due to leakage (see **Figure S5** in the SI for ferroelectric polarization data obtained on films on (001)–oriented STO:Nb substrate).[19,21,25] The impact of the total film thickness on the ferroelectric properties was not investigated due to issues related to short–circuiting the capacitor structure during sputter deposition of the Au top electrodes (for thinner films) and voltage limitations (±12 V) of the ferroelectric testing system (for thicker films). Panel (a) of **Figure 5** shows a typical polarization–electric field (*P*–*E*) hysteresis loop at 400 Hz switching frequency; the measured polarization switching currents are also shown, for clarity. The maximum applied voltage across the top and bottom electrodes was 7 V, corresponding to a maximum field of 700 kV cm^{-1}. From these dynamic *P*–*E* data, we obtain a saturation polarization $P_s \approx 34$ μC cm^{-2} (also often denoted as spontaneous polarization) and a remanent polarization $P_r \approx 25$ μC cm^{-2}. Both values are in the range reported for sol–gel derived (bulk) PZT films with similar composition, despite the fact that our material is nanostructured – the density of the mesoporous PZT should be significantly less compared to non–templated samples (note that the dielectric constant is strongly affected by introducing porosity).[67–69] The coercive field ($E_c \approx 250$ kV cm^{-1}) needed to reverse the polarization was also deduced from the hysteresis loop. A comparison with literature values is difficult, however, because E_c is known to depend on the film thickness, texture, and the strain in

the material.[70,71] Nevertheless, at first glance, the value of E_c seems slightly larger than usually observed for sol–gel derived PZT.[72]

Because both the non–remanent (volatile) polarization and leakage currents are always incorporated in *P–E* data measured in dynamic mode, thus causing an overestimation of both P_s and P_r, so–called remanent *P–E* hysteresis experiments were carried out to better characterize the remanent (switching) polarization properties. This measurement principle constitutes a small variation of the well–established PUND (Positive–Up Negative–Down) method. Here, triangular instead of rectangular pulses are applied to the sample, thereby allowing for time–resolved subtraction of the non–switching components.[73] Analysis of the data in panel (b) provides values of $P_s \approx 8$ μC cm^{-2}, $P_r \approx 7$ μC cm^{-2}, and $E_c \approx 245$ kV cm^{-1}. The factor of ~4 difference in P_s and P_r between the dynamic and remanent *P–E* data indicates that the KLE–templated PZT films suffer from comparably large parasitic capacitances and leakage currents. This, however, is not very surprising considering the microstructure and morphology. Unfortunately, it is not possible to compare our results with other data due to the lack of reports on remanent hysteresis measurements on sol–gel derived PZT thin films – typically only the values derived from dynamic *P–E* experiments are given and regarded as sufficient to describe the polarization behavior of ferroelectrics.

Panel (c) shows the *j–E* characteristics measured both under ambient conditions and in an argon–filled glove box. The fact that different top and bottom electrodes were used in this work provides an explanation for the slight asymmetry of the two branches (see also polarization switching currents in **Figure 5**).[23,24] It is well known that the electronic properties of the electrode–ferroelectric interface junctions have a profound effect on the electrical properties of the ferroelectric material. For the KLE–templated films, the Au/PZT and PZT/LSMO junctions

are likely to form Schottky–like and p–p–like contacts, respectively.[25,26] Because the leakage current behavior might be affected to some extent by adsorbed water at the solid–air interface (formation of percolating conduction pathways),[74] measurements were also conducted in an argon–filled glove box on samples vacuum dried at 120 °C for 24 h. As is evident from the data, the leakage current at high field is, in fact, reduced by more than one order of magnitude. This result demonstrates that the impact of adsorbed water from the atmosphere on the electrical properties is non–negligible and must be taken into account when dealing with porous ferroelectrics. However, to ensure comparability with data reported in the past and those of future polymer–templated nano–ferroelectrics, all polarization switching and fatigue experiments were carried out under ambient conditions.

Lastly, the fatigue behavior (remanent polarization loss during bipolar cycling) was examined to obtain insight into the endurance characteristics. Panel (d) depicts the fatigue properties of the KLE–templated PZT thin films at 400 Hz switching frequency. The respective *P*–*E* hysteresis loops after 4×10^2, 4×10^4, and 4×10^6 cycles are shown as well. As can be seen from the data, the films with Au top electrodes lost ~20% of the initial remanent polarization after 4×10^6 cycles, thereby indicating reasonable electrical endurance. Degradation phenomena are often associated with the formation and accumulation of defects – oxygen vacancies (space charge) – at the metal electrode–PZT interface (and at grain boundaries).[75–77] These otherwise "mobile" defects are pinned to the interface region and have been shown to prevent domain reversal.[75] However, this can be overcome to a large extent by using oxide top and bottom electrodes, e.g., LSMO.[21,24,26,78] In so doing, the oxygen vacancies can diffuse into the electrodes, which ultimately results in better fatigue resistance.[24,75] However, in our particular case, the use of LSMO as top electrodes was not possible because of the sputtering temperature of ~780 °C needed to obtain crystalline

material. Such a high temperature would lead to ill–defined PZT thin films due to severe restructuring of the pore network above 650 °C.

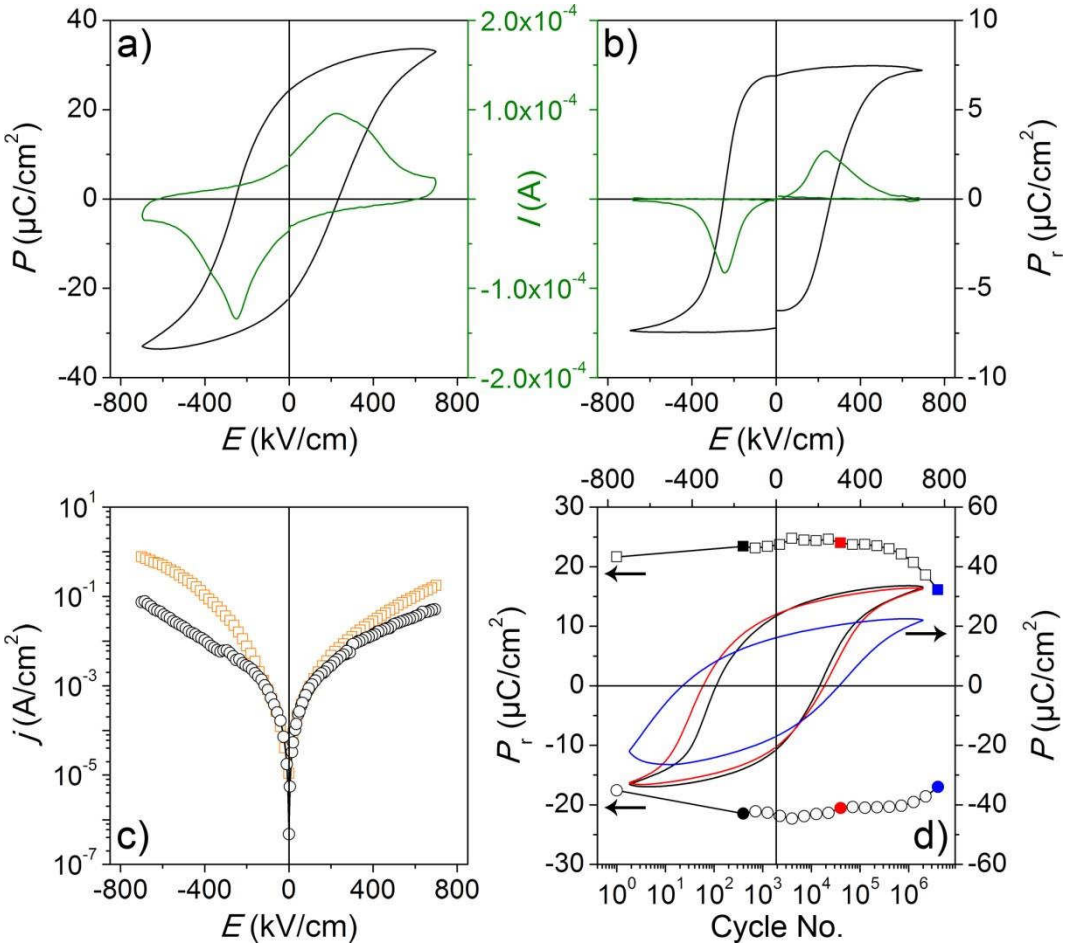

Figure 5. Ferroelectric polarization switching and fatigue behavior of KLE–templated PZT thin films on LSMO/STO:Nb heterostructure substrate heated at 650 °C for 5 min: (a) dynamic and remanent (b) *P*–*E* hysteresis loops and switching currents at 400 Hz switching frequency; (c) *j*–*E* characteristics measured under ambient conditions (orange squares) and in an argon–filled glove box (black circles); (d) fatigue properties at 400 Hz switching frequency with the respective dynamic *P*–*E* hysteresis loops after 4×10^2 (black), 4×10^4 (red), and 4×10^6 (blue) cycles.

Conclusion

Ordered mesoporous thin film ferroelectrics of PZT have been successfully prepared for the first time by evaporation–induced self–assembly. Submicrometer–thick, mesostructured films with cubic pore symmetry can be readily achieved via dip coating on (001)–oriented STO:Nb and LSMO/STO:Nb substrates when using the large diblock copolymer KLE as structure–directing agent. Microstructure studies demonstrate that the sol–gel derived material is single phase perovskite and free of impurity phases after calcination at 650 °C. They also indicate a high degree of biaxial texturing, which is unique for polymer–templated ordered mesoporous metal oxide films. The high quality of the nanocrystalline PZT samples is further confirmed by ferroelectric polarization switching experiments. Dynamic and remanent *P–E* measurements conducted on approx. 100 nm–thick films on LSMO/STO:Nb heterostructure substrate provide remanent polarization values of ~25 μC cm^{-2} and ~7 μC cm^{-2}, respectively, and a coercive field of ~250 kV cm^{-1}. The factor of ~4 difference – due to non–switching polarization and leakage current – is comparably large, but was somewhat expected. Furthermore, the films exhibit reasonable fatigue resistance, with ~80% loss of the initial remanent polarization within 4×10^6 cycles, despite the use of Au top electrodes.

In summary, this work describes a facile soft–templating route to fabricate ordered mesoporous PZT thin films with in–plane and out–of–plane preferred orientations and good electrical polarization properties. Future research will be directed towards both reducing the amount of non–switching components to further improve the overall ferroelectric performance and novel functional device design that cannot be achieved with bulk versions of this material.

AUTHOR INFORMATION

Corresponding Author

*E–mail: torsten.brezesinski@kit.edu. Phone: +49 721 608–28827.

Author Contributions

All authors have given approval to the final version of the manuscript.

Funding Sources

Financial support by the German Research Foundation (T.B., grant no. BR 3499/3–1); the Fonds der Chemischen Industrie im Verband der Chemischen Industrie through a Chemiefonds fellowship (C.R.), and the German Academic Exchange Service (T.B.) is gratefully acknowledged.

Notes

The authors declare no competing financial interest.

ASSOCIATED CONTENT

Supporting Information Available

Additional data from electron microscopy, XRR, SAXS, ToF–SIMS, and ferroelectric polarization switching measurements. This information is available free of charge via the Internet at http://pubs.acs.org.

ACKNOWLEDGMENT

We thank Ralf Witte, Dr. Thomas Leichtweiss, Dr. Jan Perlich, Dr. Marcus Rohnke, and Dr. Jan Haetge for their assistance with HRXRD, XPS, GISAXS, ToF–SIMS, and TEM imaging, respectively. Dr. Stephan Tiedke from aixACCT Systems GmbH is acknowledged for technical assistance. Portions of this research were carried out at the Justus–Liebig–University Giessen and at the light source DORIS III at DESY, a member of the Helmholtz Association (HGF).

REFERENCES

(1) Saito, Y.; Takao, H.; Tani, T.; Nonoyama, T.; Takatori, K.; Homma, T.; Nagaya, T.; Nakamura, M. *Nature* **2004**, *432*, 84–87.

(2) Rödel, J.; Jo, W.; Seifert, K. T. P.; Anton, E.-M.; Granzow, T.; Damjanovic, D. *J. Am. Ceram. Soc.* **2009**, *92*, 1153–1177.

(3) Trolier-McKinstry, S.; Muralt, P. *J. Electroceramics* **2004**, *12*, 7–17.

(4) Haertling, G. H. *J. Am. Ceram. Soc.* **1999**, *82*, 797–818.

(5) Scott, J. F. *Jpn. J. Appl. Phys.* **1999**, *38*, 2272–2274.

(6) Roelofs, A.; Schneller, T.; Szot, K.; Waser, R. *Nanotechnology* **2003**, *14*, 250–253.

(7) Moazzami, R.; Hu, C.; Shepherd, W. H. *IEEE Trans. Electron Devices* **1992**, *39*, 2044–2049.

(8) Jeon, Y. B.; Sood, R.; Jeong, J. -h.; Kim, S.-G. *Sensors Actuators A Phys.* **2005**, *122*, 16–22.

(9) Chen, X.; Xu, S.; Yao, N.; Shi, Y. *Nano Lett.* **2010**, *10*, 2133–2137.

(10) Klicker, K. A.; Biggers, J. V.; Newnham, R. E. *J. Am. Ceram. Soc.* **1981**, *64*, 5–9.

(11) Brooks, K.; Damjanovic, D.; Kholkin, A.; Reaney, I.; Setter, N.; Luginbuhl, P.; Racine, G.-A.; de Rooij, N. F.; Saaman, A. *Integr. Ferroelectr.* **1995**, *8*, 13–23.

(12) Ma, B.; Liu, S.; Gan, Z.; Liu, G.; Cai, X.; Zhang, H.; Yang, Z. *Microfluid. Nanofluidics* **2006**, *2*, 417–423.

(13) Yamamoto, T. *Jpn. J. Appl. Phys.* **1996**, *35*, 5104–5108.

(14) Fan, H.; Kim, H.-E. *J. Appl. Phys.* **2002**, *91*, 317.

(15) Lefki, K.; Dormans, G. J. M. *J. Appl. Phys.* **1994**, *76*, 1764.

(16) Guo, R.; Cross, L.; Park, S.-E.; Noheda, B.; Cox, D.; Shirane, G. *Phys. Rev. Lett.* **2000**, *84*, 5423–5426.

(17) Damjanovic, D. *Reports Prog. Phys.* **1998**, *61*, 1267–1324.

(18) Pintilie, L.; Lisca, M.; Alexe, M. *J. Optoelectron. Adv. Mater.* **2006**, *8*, 7–12.

(19) Leufke, P. M.; Kruk, R.; Wang, D.; Kübel, C.; Hahn, H. *AIP Adv.* **2012**, *2*, 032184.

(20) Ray, S. C.; Algueró, M.; Ricote, J.; Calzada, M. L.; Prieto, C.; de Andrés, A.; Garcia-Hernández, M. *Mater. Lett.* **2006**, *60*, 1714–1718.

(21) Wu, W.; Wong, K. H.; Mak, C. L.; Choy, C. L.; Zhang, Y. H. *J. Vac. Sci. Technol. A Vacuum, Surfaces, Film.* **2000**, *18*, 2412.

(22) Lu, L.; Lai, M. O.; Rüdiger, A.; Waser, R. *J. Alloys Compd.* **2008**, *449*, 2–6.

(23) Lee, J.; Ramesh, R.; Keramidas, V. G.; Warren, W. L.; Pike, G. E.; Evans, J. T. *Appl. Phys. Lett.* **1995**, *66*, 1337.

(24) Aggarwal, S.; Dhote, A. M.; Ramesh, R.; Warren, W. L.; Pike, G. E.; Dimos, D.; Raymond, M. V.; Tuttle, B. A.; Evans, J. T. *Appl. Phys. Lett.* **1996**, *69*, 2540.

(25) Juan, P. C.; Chou, H. C.; Lee, J. Y. M. *Microelectron. Reliab.* **2005**, *45*, 1003–1006.

(26) Chen, F.; Liu, Q. Z.; Wang, H. F.; Zhang, F. H.; Wu, W. *Appl. Phys. Lett.* **2007**, *90*, 192907.

(27) Kresge, C. T.; Leonowicz, M. E.; Roth, W. J.; Vartuli, J. C.; Beck, J. S. *Nature* **1992**, *359*, 710–712.

(28) Lu, Y.; Ganguli, R.; Drewien, C. A.; Anderson, M. T.; Brinker, C. J.; Gong, W.; Guo, Y.; Soyez, H.; Dunn, B.; Huang, M. H.; Zink, J. I. *Nature* **1997**, *389*, 364–368.

(29) Brinker, C. J.; Lu, Y.; Sellinger, A.; Fan, H. *Adv. Mater.* **1999**, *11*, 579–585.

(30) Thomas, A.; Schlaad, H.; Smarsly, B.; Antonietti, M. *Langmuir* **2003**, *19*, 4455–4459.

(31) Grosso, D.; Boissière, C.; Smarsly, B.; Brezesinski, T.; Pinna, N.; Albouy, P. A.; Amenitsch, H.; Antonietti, M.; Sanchez, C. *Nat. Mater.* **2004**, *3*, 787–792.

(32) Smarsly, B.; Grosso, D.; Brezesinski, T.; Pinna, N.; Boissière, C.; Antonietti, M.; Sanchez, C. *Chem. Mater.* **2004**, *16*, 2948–2952.

(33) Smarsly, B.; Antonietti, M. *Eur. J. Inorg. Chem.* **2006**, *2006*, 1111–1119.

(34) Sanchez, C.; Boissière, C.; Grosso, D.; Laberty, C.; Nicole, L. *Chem. Mater.* **2008**, *20*, 682–737.

(35) Fujita, S.; Inagaki, S. *Chem. Mater.* **2008**, *20*, 891–908.

(36) Mann, S. *Nat. Mater.* **2009**, *8*, 781–792.

(37) Ren, Y.; Ma, Z.; Bruce, P. G. *Chem. Soc. Rev.* **2012**, *41*, 4909–4927.

(38) Rawolle, M.; Niedermeier, M. A.; Kaune, G.; Perlich, J.; Lellig, P.; Memesa, M.; Cheng, Y.-J.; Gutmann, J. S.; Müller-Buschbaum, P. *Chem. Soc. Rev.* **2012**, *41*, 5131–5142.

(39) Innocenzi, P.; Malfatti, L. *Chem. Soc. Rev.* **2013**, *42*, 4198–4216.

(40) Petkovich, N. D.; Stein, A. *Chem. Soc. Rev.* **2013**, *42*, 3721–3739.

(41) Deng, Y.; Wei, J.; Sun, Z.; Zhao, D. *Chem. Soc. Rev.* **2013**, *42*, 4054–4070.

(42) Gu, D.; Schüth, F. *Chem. Soc. Rev.* **2013**, *43*, 313–344.

(43) Leufke, P. M.; Mishra, A. K.; Beck, A.; Wang, D.; Kübel, C.; Kruk, R.; Hahn, H. *Thin Solid Films* **2012**, *520*, 5521–5527.

(44) Schlaad, H.; Kukula, H.; Rudloff, J.; Below, I. *Macromolecules* **2001**, *34*, 4302–4304.

(45) Oveisi, H.; Jiang, X.; Imura, M.; Nemoto, Y.; Sakamoto, Y.; Yamauchi, Y. *Angew. Chem. Int. Ed.* **2011**, *123*, 7548–7551.

(46) Müller-Buschbaum, P. *Anal. Bioanal. Chem.* **2003**, *376*, 3–10.

(47) Disch, S.; Wetterskog, E.; Hermann, R. P.; Salazar-Alvarez, G.; Busch, P.; Brückel, T.; Bergström, L.; Kamali, S. *Nano Lett.* **2011**, *11*, 1651–1656.

(48) Tate, M. P.; Hillhouse, H. W. *J. Phys. Chem. C* **2007**, *111*, 7645–7654.

(49) Hanrath, T.; Choi, J. J.; Smilgies, D.-M. *ACS Nano* **2009**, *3*, 2975–2988.

(50) Brezesinski, T.; Antonietti, M.; Smarsly, B. M. *Adv. Mater.* **2007**, *19*, 1074–1078.

(51) Reitz, C.; Suchomski, C.; Weidmann, C.; Brezesinski, T. *Nano Res.* **2011**, *4*, 414–424.

(52) Reitz, C.; Haetge, J.; Suchomski, C.; Brezesinski, T. *Chem. Mater.* **2013**, *25*, 4633–4642.

(53) Choi, S. Y.; Mamak, M.; Coombs, N.; Chopra, N.; Ozin, G. A. *Adv. Funct. Mater.* **2004**, *14*, 335–344.

(54) Reitz, C.; Suchomski, C.; Haetge, J.; Leichtweiss, T.; Jagličić, Z.; Djerdj, I.; Brezesinski, T. *Chem. Commun.* **2012**, *48*, 4471–4473.

(55) Zhu, Z.-X.; Li, J.-F.; Lai, F.-P.; Zhen, Y.; Lin, Y.-H.; Nan, C.-W.; Li, L.; Li, J. *Appl. Phys. Lett.* **2007**, *91*, 222910.

(56) Zhao, J.; Lu, L.; Thompson, C. V.; Lu, Y. F.; Song, W. D. *J. Cryst. Growth* **2001**, *225*, 173–177.

(57) Zanetti, S.; Leite, E.; Longo, E.; Varela, J. *Mater. Res.* **2001**, *4*, 157–162.

(58) Qi, X.; Dho, J.; Blamire, M.; Jia, Q.; Lee, J.-S.; Foltyn, S.; MacManus-Driscoll, J. L. *J. Magn. Magn. Mater.* **2004**, *283*, 415–421.

(59) Zhu, T. J. *J. Appl. Phys.* **2004**, *95*, 241.

(60) Hu, Z.; Gu, H.; Hu, Y.; Zou, Y.; Zhou, D. *Mater. Chem. Phys.* **2009**, *113*, 42–45.

(61) Chu, M.-W.; Ganne, M.; Caldes, M. T.; Brohan, L. *J. Appl. Phys.* **2002**, *91*, 3178.

(62) Nyholm, R.; Martensson, N.; Lebugle, A.; Axelsson, U. *J. Phys. F Met. Phys.* **1981**, *11*, 1727–1733.

(63) Gong, W.; Li, J.-F.; Chu, X.; Gui, Z.; Li, L. *Acta Mater.* **2004**, *52*, 2787–2793.

(64) Wakiya, N.; Kuroyanagi, K.; Xuan, Y.; Shinozaki, K.; Mizutani, N. *Thin Solid Films* **2000**, *372*, 156–162.

(65) Wagner, C. D.; Davis, L. E.; Zeller, M. V.; Taylor, J. A.; Raymond, R. H.; Gale, L. H. *Surf. Interface Anal.* **1981**, *3*, 211–225.

(66) Lefevre, M. J.; Speck, J. S.; Schwartz, R. W.; Dimos, D.; Lockwood, S. J. *J. Mater. Res.* **2011**, *11*, 2076–2084.

(67) Nakamura, T.; Nakao, Y.; Kamisawa, A.; Takasu, H. *Appl. Phys. Lett.* **1994**, *65*, 1522.

(68) Zeng, T.; Dong, X.; Mao, C.; Zhou, Z.; Yang, H. *J. Eur. Ceram. Soc.* **2007**, *27*, 2025–2029.

(69) Banno, H. *Jpn. J. Appl. Phys.* **1993**, *32*, 4214–4217.

(70) Scott, J. F.; Kammerdiner, L.; Parris, M.; Traynor, S.; Ottenbacher, V.; Shawabkeh, A.; Oliver, W. F. *J. Appl. Phys.* **1988**, *64*, 787.

(71) Dawber, M.; Rabe, K. M.; Scott, J. F. *Rev. Mod. Phys.* **2005**, *77*, 1083–1130.

(72) Barrow, D. A.; Petroff, T. E.; Tandon, R. P.; Sayer, M. *J. Appl. Phys.* **1997**, *81*, 876.

(73) Bornand, V.; Trolier-McKinstry, S.; Takemura, K.; Randall, C. A. *J. Appl. Phys.* **2000**, *87*, 3965.

(74) Han, M.; Youssef, S.; Rosenberg, E.; Fleury, M.; Levitz, P. *Phys. Rev. E* **2009**, *79*, 031127.

(75) Friessnegg, T.; Aggarwal, S.; Ramesh, R.; Nielsen, B.; Poindexter, E. H.; Keeble, D. J. *Appl. Phys. Lett.* **2000**, *77*, 127.

(76) Lee, J.; Desu, S. B. *Ferroelectr. Lett. Sect.* **1995**, *20*, 27–34.

(77) Chen, F.; Schafranek, R.; Wu, W.; Klein, A. *J. Phys. D. Appl. Phys.* **2009**, *42*, 215302.

(78) Schorn, P. J.; Bräuhaus, D.; Böttger, U.; Waser, R.; Beitel, G.; Nagel, N.; Bruchhaus, R. *J. Appl. Phys.* **2006**, *99*, 114104.

TOC graphic

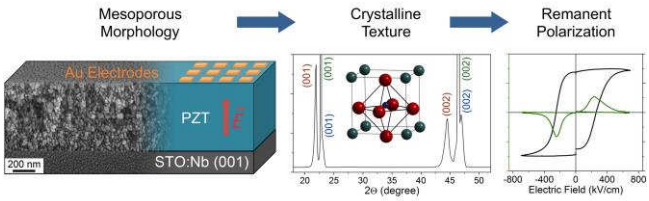
Mesoporous Morphology
Crystalline Texture
Remanent Polarization
Au Electrodes
PZT
STO:Nb (001)
200 nm
(001)
(002)
2θ (degree)
Electric Field (kV/cm)